ADVANCED FUNCTIONAL MATERIALS
www.afm-journal.de

Graphene/Strontium Titanate: Approaching Single Crystal–Like Charge Transport in Polycrystalline Oxide Perovskite Nanocomposites through Grain Boundary Engineering

Yue Lin, Maxwell Thomas Dylla, Jimmy Jiahong Kuo, James Patrick Male, Ian Anthony Kinloch, Robert Freer, and Gerald Jeffery Snyder**

Grain boundaries critically limit the electronic performance of oxide perovskites. These interfaces lower the carrier mobilities of polycrystalline materials by several orders of magnitude compared to single crystals. Despite extensive effort, improving the mobility of polycrystalline materials (to meet the performance of single crystals) is still a severe challenge. In this work, the grain boundary effect is eliminated in perovskite strontium titanate (STO) by incorporating graphene into the polycrystalline microstructure. An effective mass model provides strong evidence that polycrystalline graphene/strontium titanate (G/STO) nanocomposites approach single crystal-like charge transport. This phenomenological model reduces the complexity of analyzing charge transport properties so that a quantitative comparison can be made between the nanocomposites and STO single crystals. In other related works, graphene composites also optimize the thermal transport properties of thermoelectric materials. Therefore, decorating grain boundaries with graphene appears to be a robust strategy to achieve "phonon glass–electron crystal" behavior in oxide perovskites.

1. Introduction

Oxide perovskites have received intensive research interest due to a broad spectrum of functional properties linked to their electronic structure. These include high temperature superconductivity,[1] ferroelectricity,[2] the colossal magnetoeffect,[3] and many other attractive properties.[4] Because of these properties, oxide perovskites are promising candidates for thermoelectricity,[5] catalysis,[6] fuel cells,[7] and solar cells.[8] High-mobility electronic transport is crucial for all these applications. As single crystals, oxide perovskites meet the high mobility design requirement.[9] However, the growth of single crystals is considerably expensive and challenging.[10] From the perspective of real-world applications, polycrystalline oxide perovskites are significantly more cost effective compared to single crystals. Hence, polycrystalline oxide perovskites will be more attractive for real-world applications if their electronic performance approaches that of single crystals. Enhancing charge transport of polycrystalline oxide perovskites is therefore a key area to explore.[11] Despite extensive efforts, the carrier mobilities of polycrystalline oxide perovskites are usually orders of magnitude less than the carrier mobilities in single crystals.[11] The existence of grain boundaries plays a major role in this mobility reduction[12,13] (**Figure 1**) due to grain boundary effects that also exist in other perovskite materials,[14] as well as magnesium antimonide.[15]

Here, we demonstrate a solution to eliminate the grain boundary effect and improve charge transport in a polycrystalline oxide perovskite by adding graphene. By applying an effective mass model, we reveal that the structurally polycrystalline graphene/strontium titanate (G/STO) nanocomposites exhibit single crystal-like electronic transport behavior. This discovery suggests that graphene/oxide perovskite nanocomposites are promising candidates for many of the aforementioned applications.

2. Results and Discussion

2.1. Structure Analysis of G/STO Nanocomposites

Two necessary aspects for high-quality G/STO nanocomposite synthesis were carefully monitored in this experimental synthesis. First, the samples should be fully densified. Measured densities of the sintered pristine STO, 0.11 vol% G/STO and 0.22 vol% G/STO were 4.972, 4.967, and 4.959 g cm^{-3},

Dr. Y. Lin
Cavendish Laboratory
University of Cambridge
J. J. Thomson Avenue, Cambridge CB3 0HE, UK
E-mail: yl589@cam.ac.uk
Dr. Y. Lin, Dr. M. T. Dylla, J. J. Kuo, J. P. Male, Prof. G. J. Snyder
Department of Materials Science and Engineering
Northwestern University
Evanston, IL 60208, USA
E-mail: jeff.snyder@northwestern.edu
Prof. I. A. Kinloch, Prof. R. Freer
The School of Materials
University of Manchester
Oxford Road, Manchester M13 9PL, UK
The ORCID identification number(s) for the author(s) of this article can be found under https://doi.org/10.1002/adfm.201910079.

DOI: 10.1002/adfm.201910079

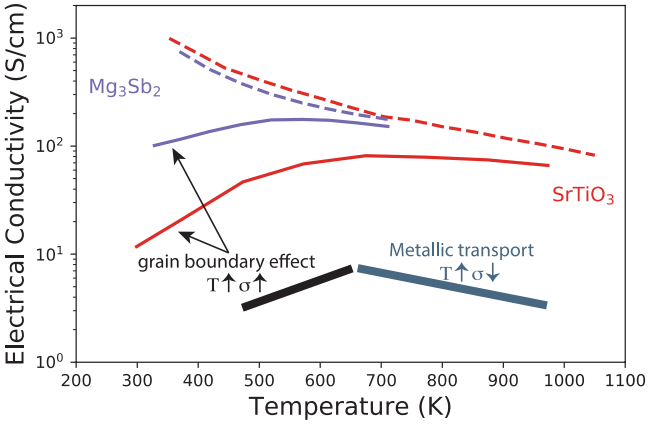

Figure 1. The electrical conductivity of strontium titanate and magnesium antimonide both suffer from the effect of grain boundaries. Charge transport in the polycrystalline materials (solid lines) is limited by the grain boundaries and is significantly worse than single crystals (dashed lines). Notice that the polycrystalline samples show activated conductivity with temperature. By contrast, electrical conductivities of the single-crystal samples decrease monotonically with temperature. In this comparison, the carrier concentration of polycrystalline and single crystal samples for each material have the same carrier concentration. Te doped Mg_3Sb_2: 3.0×10^{19} cm^{-3}, and La doped $SrTiO_3$: 8.4×10^{20} cm^{-3}. Literature data sources: Mg_3Sb_2,[15,16] $SrTiO_3$.[17,18]

respectively, confirming full densification over 97% of theoretical density (5.110, 5.107, and 5.104 g cm^{-3}, respectively) in each sample. As a second requirement, the graphene sheets need to survive the harsh sintering process and be uniformly dispersed in the STO matrix after sintering. The presence of graphene in the composites was confirmed by scanning electron microscopy (SEM, **Figure 2**b; Figure S1, Supporting Information) and transmission electron microscopy (TEM) (Figure 2c–e). Both techniques reveal graphene sheets homogenously distributed at the grain boundaries without localized aggregation. Raman spectroscopy performed on sintered pellets (Figure 2f) shows a pattern of few layer graphene,[19] further confirming graphene incorporation without structural degradation or aggregation into graphite. In the spectra, the D band at ≈1340 cm^{-1} represents a disordered or defective carbon structure and is indicative of the edges of graphene sheets. The G band at ≈1580 cm^{-1} represents sp^2 carbon hexagonal networks connected by covalent bonds that form the undefective structure of graphene.[20] The D to G band ratio (I_D/I_G) is a strong indication of the defect concentration in graphene samples. The D to G band ratios of both the as-prepared graphene sheets and the graphene sheets in the nanocomposites are ≈0.25, indicating the composite processing steps did not induce defects to the graphene sheets. A closer inspection of the spectra reveals that the full width at half maximum of the G band increases significantly, from 18 cm^{-1} for as-prepared graphene sheets to 30 cm^{-1} for the graphene sheets in the nanocomposites. This G band widening is accounted for by the curvature of graphene sheets,[19] which is confirmed by electron microscopy (Figure 2b; Figure S1b, Supporting Information). X-ray diffraction (XRD) on sintered pellets (Figure 2g) was also employed to provide additional structural information on the matrix phase in each sample. XRD patterns show a combination of 36% Pm-3m cubic phase ($SrTiO_3$) and 64% P4/mmm tetragonal phase ($SrTiO_{2.6}$) for both pristine STO and the nanocomposites.

2.2. Motivation to Investigate Transport Properties with an Effective Mass Model

The electronic properties of oxide perovskites (such as STO) vary significantly with Fermi energy (E) and carrier concentration (n), which can be modified by processing. For example, STO can be doped with extrinsic dopants like lanthanum or niobium to increase the carrier concentration, and therefore, the electrical conductivity. Additionally, when samples are sintered under a reducing environment, doubly charged oxygen vacancies contribute additional charge carriers.[21] Due to the charge carrier concentration dependence of transport properties, it is difficult to separate carrier density effects from those of grain boundaries. A more direct way to investigate the quality of electronic transport is with an effective mass model.[22] With this model, one can estimate latent variables that underpin measured quantities such as the electrical conductivity and the Seebeck coefficient. One of these latent variables is the weighted mobility (μ_w), which is a carrier concentration-independent quantity. With weighted mobility, one can decouple the effects of grain boundaries from the effects of carrier concentration (see Supporting Information for the derivation). In theory, weighted mobility is a composite property, composed of the effective mass relative to the free electron mass (m^*/m_e) and the mobility parameter (μ_0). The effective mass quantifies the number of conduction channels for electronic transport, and the mobility parameter quantifies the mobility of those conduction channels.

$$\mu_w = \mu_0 \left(\frac{m^*}{m_e} \right)^{3/2} \tag{1}$$

The mobility parameter is related to the relaxation time of the free carriers (τ_0) through the elementary electric charge (e) and the effective mass.

$$\mu_0 = \frac{\tau_0 e}{m^*} \tag{2}$$

Consider the transport properties of several STO single crystals from the literature. These samples were doped by various extrinsic elements and/or a reducing atmosphere (generating oxygen vacancies). Although the electrical conductivity (**Figure 3**a), Seebeck coefficient (Figure 3b), and power factor (Figure 3c) vary significantly between samples (due to different doping levels), the weighted mobilities are nearly identical (Figure 3d). Furthermore, the weighted mobility decreases with temperature as $T^{-3/2}$, which indicates acoustic phonon scattering. It is well known from the literature that acoustic phonon scattering limits the mobility of STO single crystals.[23] By contrast, consider the transport properties of several polycrystalline STO samples from the literature. Below 600 K, the weighted mobility is thermally activated and much lower than in the STO single crystals (Figure 3d), indicating that grain boundaries are reducing mobility. The grain boundary effect is further corroborated by the raw transport measurements. The signature of the grain boundary effect in

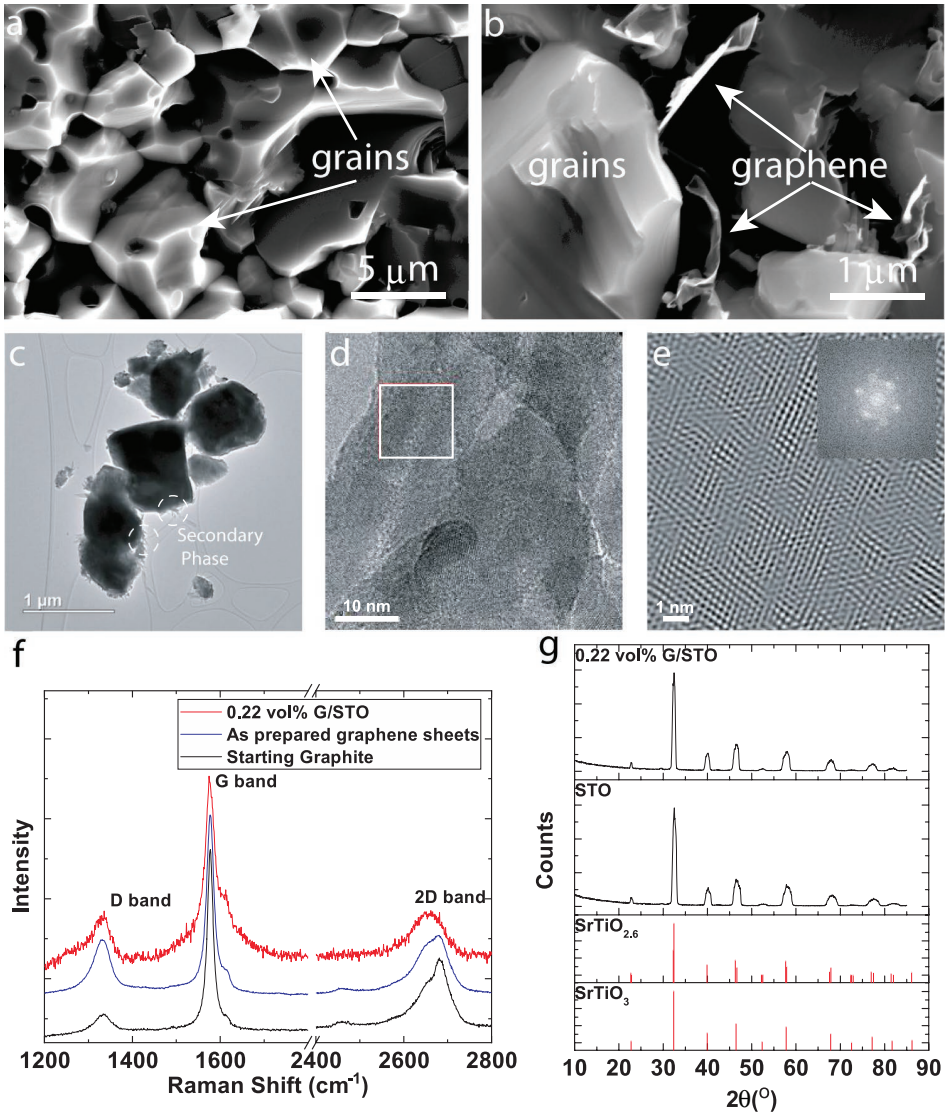

Figure 2. Structural characterization of the STO and its nanocomposites incorporated with graphene. a–e) Microscopic characterization. a,b) SEM images of a fracture surface of STO and the 0.22 vol% G/STO nanocomposite. c–e) TEM images of a crushed 0.22 vol% G/STO nanocomposite. c) A secondary phase found at the edges of the crushed grains is indicated by dashed white circles. d,e) High-resolution (HR) TEM images of the secondary phase identify the phase as graphene. e) HRTEM image of white square area in (d), showing the repeating honeycomb features of graphene. The inset image shows the diffraction pattern. f) Raman spectra showing non-defective graphene indicators in the D and G band. The Raman spectra is an average of 10 scans at different sample locations with a spot size of 5 µm. g) XRD pattern on sintered pellets of both pristine STO and 0.22 vol% G/STO. Both patterns show the same mix of $SrTiO_3$ and the reduced $SrTiO_{2.6}$ phase.

these materials is electrical conductivity that is activated with temperature (Figure 3a), and a Seebeck coefficient (the absolute value) that increases gradually with temperature (Figure 3b).[13,15] Essentially, the conductivity is affected by grain boundaries, while the Seebeck coefficient is not. The relative weighted mobility between polycrystalline samples and single crystal samples indicates the strength of the grain boundary effect.

2.3. Weighted Mobilities of G/STO Nanocomposites

The electrical conductivity of pristine STO (**Figure 4**a) is less than 1 S cm^{-1} and is thermally activated. With the addition of graphene, two trends are observed. First, graphene boosts the electrical conductivity of STO nanocomposites, and second, the thermally activated behavior shifts towards lower temperatures. Furthermore, the 0.22 vol% G/STO, 0.23 vol% G/LSTO, and 0.23 vol% reduced graphene oxide (RGO)/NSTO nanocomposites show fully metallic transport behavior, where the electrical conductivity decreases with increasing temperature over the entire temperature range. Adding graphene eliminates the activated conductivity, which means that it eliminates the detrimental effect of grain boundaries on transport. By examining electrical conductivity alone, one cannot conclude that the charge transport behavior of the polycrystalline graphene/STO nanocomposites matches the transport properties of single

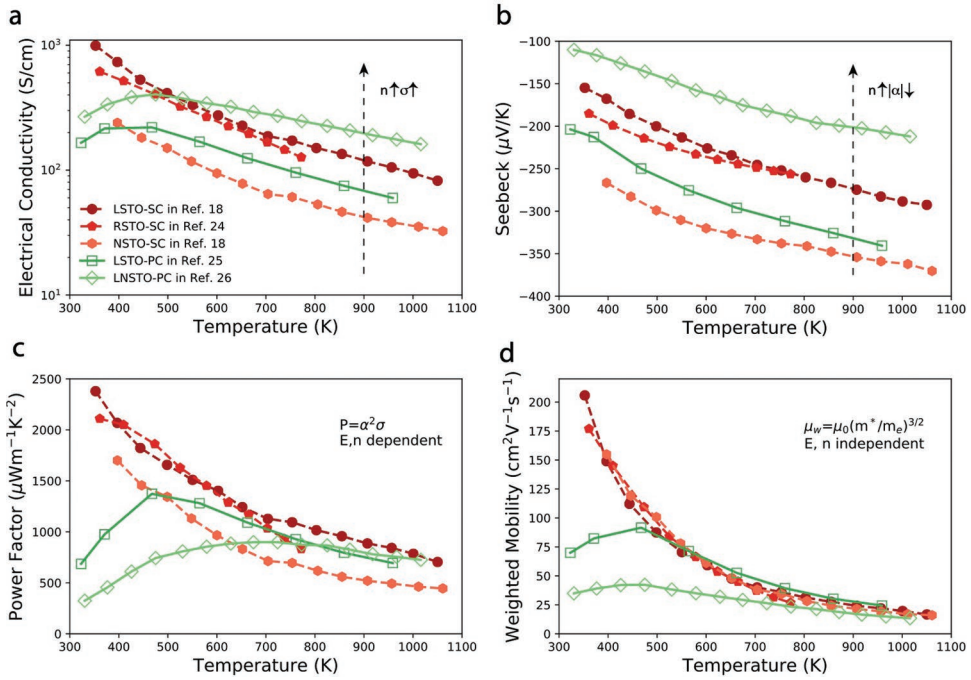

Figure 3. a) Electrical conductivity, σ, b) Seebeck coefficient, α, c) power factor, P, and d) weighted mobility, μ_w of STO perovskite oxides from literature sources. Electrical conductivity and Seebeck coefficient are strongly dependent on Fermi energy (E) and carrier concentration (n). Thus, the power factor ($\alpha^2\sigma$) is carrier concentration-dependent as well. Weighted mobility is carrier concentration-independent and reflects intrinsic charge transport, which makes it ideal for comparing samples prepared under different processing conditions. Single crystals (SC) are indicated with red dashed lines and polycrystalline samples (PC) are indicated with green solid lines. Literature sources: lanthanum doped STO single crystal (LSTO-SC),[18] reduced STO single crystal (RSTO-SC),[24] niobium doped STO single crystal (NSTO-SC),[18] polycrystalline lanthanum doped STO (LSTO-PC),[25] polycrystalline lanthanum and niobium doped STO (LNSTO-PC).[26]

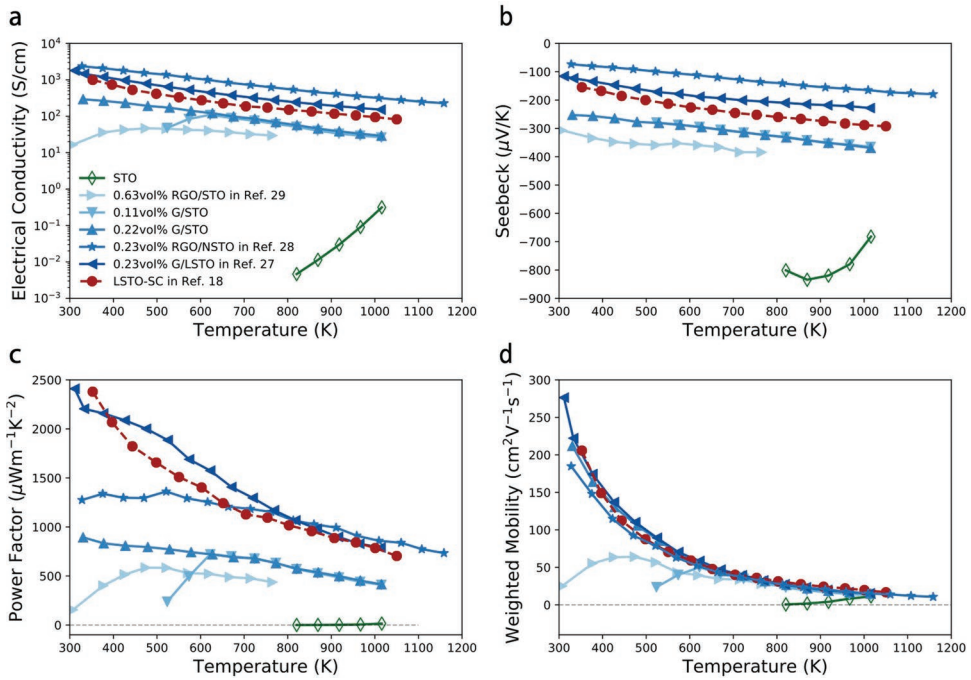

Figure 4. a) Electrical conductivity, σ, b) Seebeck coefficient, α, c) power factor, P, and d) weighted mobility μ_w of single crystal LSTO, polycrystalline STO, and STO nanocomposites with graphene. Below 800 K the electrical conductivity and the Seebeck coefficient of polycrystalline STO (without graphene) are beyond the limits of the instruments used here. Literature data sources: lanthanum doped STO single crystal (LSTO SC),[18] reduced graphene oxide/STO nanocomposite (RGO/STO),[29] graphene/lanthanum doped STO nanocomposite (G/LSTO),[27] reduced graphene oxide/niobium doped STO nanocomposite (RGO/NSTO).[28]

crystals, since electrical conductivity depends on carrier concentration (as discussed in previous session). In fact, the 0.23 vol% RGO/NSTO and G/LSTO samples have higher electrical conductivities than the LSTO single crystalline sample. The cause of the higher conductivities in the nanocomposites is their higher carrier concentrations (7.23×10^{20} cm^{-3} in RGO/NSTO and 8.4×10^{20} cm^{-3} in G/LSTO) compared to the single crystal sample (6.8×10^{20} cm^{-3}).

The weighted mobility analysis unequivocally shows that the best nanocomposites have the same intrinsic charge transport characteristics as the single crystal (Figure 4d). The grain boundary effect is significantly reduced with the addition of only 0.11 vol% pristine graphene, and the weighted mobility matches that of single crystals above 700 K. At higher graphene concentrations (around 0.22 vol%,) the grain boundary effect is completely eliminated above room temperature. The weighted mobilities of the G/STO, G/LSTO,[27] and RGO/NSTO[28] nanocomposites are the same as that of STO single crystals. This observation suggests the charge transport in the nanocomposites is now governed by acoustic phonon scattering, whereas without graphene, grain boundary scattering limits the mobility in the low temperature range. The 0.63 vol% RGO/STO nanocomposite[29] similarly reduces the overall grain boundary effect. It is worth pointing out that Nam[30] et al. also reported similar behavior in aluminum doped zinc oxide (AZO)/(RGO) nanocomposites. The AZO/RGO nanocomposites exhibit single crystal-like Hall mobility in nanograin samples. With such a high concentration of interfaces, electron transport could be hindered by scattering from trapped charges at the grain boundaries. They contribute the lack of scattering to weakened grain boundary barriers and the proper band alignment between the AZO and RGO. Thus, electrons can freely conduct across the nanograin boundaries in their samples.

2.4. Discussion on Charge Transport Mechanism

Evidence from this study as well as the literature suggests that the improved electronic transport properties of the nanocomposites are a result of point-defect engineering at the grain boundaries. In pristine STO (without graphene) there are low oxygen vacancy concentrations near the grain boundaries.[31] The depletion of positively charged oxygen vacancies induces a negative potential that perturbs the electronic states in the conduction band. As a result, the grain boundary phase is depleted of free carriers and becomes more resistive (**Figure 5**).[13] With the addition of graphene, the formation of oxygen vacancies is promoted in the grain boundary regions adjacent to the interfacial graphene, resulting in a localized rise in carrier concentration.[29] In this context, graphene may be acting as a chemical reducing agent for the STO matrix. With the addition of graphene (Table S2, Supporting Information), we observed an increase in bulk carrier concentration as well as significant enhancement in charge carrier mobility. Okhay et al.[28] and Rahman et al.[32] also overserved a similar effect. These observations indicate reduction or even elimination of the depletion regions across grain boundaries by increased oxygen vacancy concentrations.

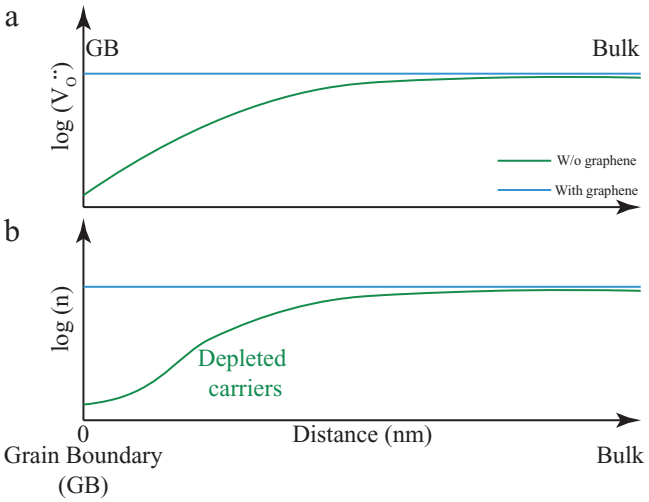

Figure 5. The lower oxygen vacancy concentrations ($V_O^{\cdot\cdot}$) in the a) grain boundary regions result in free carrier (n) depletion at b) grain boundaries. Thus, the grain boundaries become resistive. Graphene promotes the formation of oxygen vacancies in the vicinity of grain boundaries adjacent to the graphene, resulting in localized increases in carrier concentration.

3. Conclusion and Outlooks

In summary, grain boundaries are a major limiting factor for electronic transport in oxide perovskites at low temperatures. The incorporation of graphene into STO eliminates the grain boundary effect. By analyzing transport data from this work as well as the literature, we demonstrate that structurally polycrystalline G/STO nanocomposites behave electronically like single crystals. Furthermore, the incorporation of graphene or carbon nanotubes has been shown to be an effective strategy for reducing the thermal conductivity of perovskite STO[27–29] and other semiconducting materials, including skutterudite[33] and Cu_2Se.[34] Thus, decorating grain boundaries with graphene appears to be a robust strategy towards a creating a "phonon glass–electron crystal,"[35] which is particularly useful for thermoelectric applications. This discovery of a structurally polycrystalline, electronically single crystalline G/STO nanocomposite also demonstrates a new hybrid strategy for developing high performance oxide perovskite materials for applications such as fuel cells and solar cells. Thus, we encourage the community to further explore applications of graphene in oxide perovskite materials.

4. Experimental Section

Materials: STO nanopowder (chemical composition: $SrTiO_3$, 99% purity with trace metal basis, <100 nm particle size) was purchased from Sigma-Aldrich, UK. Graphene (G) was produced by exfoliating nanographite platelets (xGnP M-5) purchased from XG Sciences Ltd. All solvents were purchased from Sigma-Aldrich, UK. Cetyltrimethylammonium bromide for exfoliation of nanographite platelets was also obtained from Sigma-Aldrich, UK.

Preparation of G/STO Nanocomposites: Exfoliation of graphene nanoplatelets into graphene sheets was achieved following a liquid phase exfoliation method.[36] The graphene sheets were dispersed in water at a concentration of 1 mg mL^{-1} with assistance from tip

sonication for 30 min. STO powders were similarly dispersed in water with a concentration of 100 mg mL^{-1} by sonication for 30 min. In order to yield target compositions, calculated amounts of the graphene dispersion and the STO dispersion were mixed by mechanical stirring for 30 min, followed by sonication for another 30 min. The resultant mixture was then filtered and dried in a vacuum oven at 80 °C overnight. The dried powders were then milled in a planetary mill at 1000 rpm for 3 h. Milled powders were then pressed into pellets with diameter of 20 mm and thickness of 5 mm. The pressed pellets were sintered at 1427 °C (1700 K) under an atmosphere of 95% argon and 5% hydrogen for 24 h.

Structural Characterization: Density (ρ) of the sintered samples was determined by the Archimedes method. Raman spectra were taken using a Renishaw 2000 Raman spectrometer system and a HeNe laser (1.96 eV, 633 nm). Microstructures of the STO and its nanocomposites with graphene were investigated by SEM (Philips XL30 FEGSEM). XRD spectra were obtained by employing a Philips automatic powder diffractometer (APD, copper anode at 50 kV and filament current 40 mA). The samples were scanned from 10° to 85° with a step size of 0.02° and a scan speed of 0.0025° s^{-1}. The electrical conductivity (σ) and Seebeck coefficient (α) were determined simultaneously using an ULVAC-RIKO ZEM-3 system under a helium atmosphere. The Hall coefficient measurements were performed at room temperature using a homebuilt instrument employing 4-point probe van der Pauw methodology with a 0.8 T magnetic field.[37]

Method of Weighted Mobility Analysis: Evaluation of μ_w can be done through Seebeck-conductivity data, without needing to know a material's carrier concentration.

The Seebeck coefficient of a semiconductor can be expressed as:

$$S = \frac{k_B}{e}\left[\frac{(s+1)F_s(\eta)}{sF_{s-1(\eta)}} - \eta\right] \tag{3}$$

Here, k_B is Boltzmann's constant, e is elementary charge, η is reduced chemical potential, and F_s is the Fermi–Dirac integral given a certain scattering mechanism represented by s.

Electrical conductivity of a semiconductor can be expressed as:

$$\sigma = \sigma_{E_0}(T) \times sF_{s-1}(\eta) \tag{4}$$

Where the transport coefficient, σ_{E0}, can be expressed as:

$$\sigma_{E_0} = \frac{e(2m_e k_B T)^{3/2}}{3\pi^2\hbar^3} \times \mu_w \tag{5}$$

Here, m_e is electron mass, and $\hbar$ is reduced Planck constant.

Acoustic phonon scattering is the major scattering mechanism for perovskite oxides, meaning $s = 1$. From the Seebeck coefficient (Equation (3)), one can solve the reduced chemical potential, η. With $s = 1$ and the calculated η, one can solve for the transport coefficient, σ_{E0} (Equation (4)), which is proportional to μ_w (Equation (5)) at a given temperature. See Supporting Information for a more detailed derivation.

Supporting Information

Supporting Information is available from the Wiley Online Library or from the author.

Acknowledgements

Y.L. and M.T.D. contributed equally to this work. This work was funded by the European Union's Horizon 2020 research and innovation programme under the Marie Skłodowska-Curie individual Fellowship programme No. 800031. The authors gratefully acknowledge the support provided by the EPSRC (awards: EP/I036230/1, EP/L014068/1, and EP/L017695/1). The authors would also like to acknowledge funding from the National Science Foundation (DMREF-1729487 and DMREF-1333335). This work was performed under the following financial assistance award 70NANB19H005 from U.S. Department of Commerce, National Institute of Standards and Technology as part of the Center for Hierarchical Materials Design (CHiMaD). As the Research Chair in Carbon Materials, I.A.K. gratefully acknowledges support from Morgan Advanced Materials/ Royal Academy of Engineering.

Conflict of Interest

The authors declare no conflict of interest.

Keywords

charge transport, grain boundary engineering, graphene, nanocomposites, oxide perovskites

Received: December 2, 2019
Revised: January 2, 2020
Published online: February 3, 2020

[1] a) Y. Maeno, H. Hashimoto, K. Yoshida, S. Nishizaki, T. Fujita, J. G. Bednorz, F. Lichtenberg, *Nature* **1994**, *372*, 532; b) J. G. Bednorz, K. A. Muller, *Z. Phys. B Condens. Matter* **1986**, *64*, 189.
[2] G. A. Samara, *J. Phys.: Condens. Matter* **2003**, *15*, R367.
[3] S. Jin, T. H. Tiefel, M. Mccormack, R. A. Fastnacht, R. Ramesh, L. H. Chen, *Science* **1994**, *264*, 413.
[4] a) H. Iwahara, H. Uchida, K. Ono, K. Ogaki, *J. Electrochem. Soc.* **1988**, *135*, 529; b) K. Q. Huang, R. S. Tichy, J. B. Goodenough, *J. Am. Ceram. Soc.* **1998**, *81*, 2576; c) A. Ohtomo, H. Y. Hwang, *Nature* **2006**, *441*, 120.
[5] a) H. Somaily, S. Kolesnik, B. Dabrowski, O. Chmaissem, *Phys. Rev. B* **2017**, *96*, 064105; b) H. Ohta, *Mater. Today* **2007**, *10*, 44.
[6] H. Y. Zhu, P. F. Zhang, S. Dai, *ACS Catal.* **2015**, *5*, 6370.
[7] Y. Zhou, X. F. Guan, H. Zhou, K. Ramadoss, S. Adam, H. J. Liu, S. Lee, J. Shi, M. Tsuchiya, D. D. Fong, S. Ramanathan, *Nature* **2016**, *534*, 231.
[8] W. J. Yin, B. C. Weng, J. Ge, Q. D. Sun, Z. Z. Li, Y. F. Yan, *Energy Environ. Sci.* **2019**, *12*, 442.
[9] H. J. Kim, U. Kim, H. M. Kim, T. H. Kim, H. S. Mun, B. G. Jeon, K. T. Hong, W. J. Lee, C. Ju, K. H. Kim, K. Char, *Appl. Phys. Express* **2012**, *5*, 061102.
[10] E. Grabowska, *Appl. Catal., B* **2016**, *186*, 97.
[11] W. J. Lee, H. J. Kim, J. Kang, D. H. Jang, T. H. Kim, J. H. Lee, K. H. Kim, *Annu. Rev. Mater. Res.* **2017**, *47*, 391.
[12] a) H. J. Kim, U. Kim, T. H. Kim, J. Kim, H. M. Kim, B. G. Jeon, W. J. Lee, H. S. Mun, K. T. Hong, J. Yu, K. Char, K. H. Kim, *Phys. Rev. B* **2012**, *86*, 165205; b) A. M. Dehkordi, S. Bhattacharya, T. Darroudi, J. W. Graff, U. Schwingenschlogl, H. N. Alshareef, T. M. Tritt, *Chem. Mater.* **2014**, *26*, 2478.
[13] M. T. Dylla, J. J. Kuo, I. Witting, G. J. Snyder, *Adv. Mater. Interfaces* **2019**, *6*, 1900222.
[14] a) L. M. Herz, *ACS Energy Lett.* **2017**, *2*, 1539; b) H. D. Kim, H. Ohkita, H. Benten, S. Ito, *Adv. Mater.* **2016**, *28*, 917.
[15] J. J. Kuo, S. D. Kang, K. Imasato, H. Tamaki, S. Ohno, T. Kanno, G. J. Snyder, *Energy Environ. Sci.* **2018**, *11*, 429.
[16] T. Kanno, H. Tamaki, H. K. Sato, S. D. Kang, S. Ohno, K. Imasato, J. J. Kuo, G. J. Snyder, Y. Miyazaki, *Appl. Phys. Lett.* **2018**, *112*, 033903.
[17] I. Mahmud, M.-S. Yoon, I.-H. Kim, M.-K. Choi, S.-C. Ur, *J. Korean Phys. Soc.* **2016**, *68*, 35.
[18] S. Ohta, T. Nomura, H. Ohta, K. Koumoto, *J. Appl. Phys.* **2005**, *97*, 034106.

[19] A. C. Ferrari, J. C. Meyer, V. Scardaci, C. Casiraghi, M. Lazzeri, F. Mauri, S. Piscanec, D. Jiang, K. S. Novoselov, S. Roth, A. K. Geim, *Phys. Rev. Lett.* **2006**, *97*, 187401.
[20] L. M. Malard, M. A. Pimenta, G. Dresselhaus, M. S. Dresselhaus, *Phys. Rep.* **2009**, *473*, 51.
[21] O. N. Tufte, P. W. Chapman, *Phys. Rev.* **1967**, *155*, 796.
[22] a) A. Zevalkink, D. M. Smiadak, J. L. Blackburn, A. J. Ferguson, M. L. Chabinyc, O. Delaire, J. Wang, K. Kovnir, J. Martin, L. T. Schelhas, T. D. Sparks, S. D. Kang, M. T. Dylla, G. J. Snyder, B. R. Ortiz, E. S. Toberer, *Appl. Phys. Rev.* **2018**, *5*, 021303; b) A. F. May, G. J. Snyder, *Materials, Preparation, and Characterization in Thermoelectrics Chapter: Introduction to Modeling Thermoelectric Transport at High Temperatures*, 1st ed. **2012**, p. 552.
[23] P. A. Mante, C. C. Stoumpos, M. G. Kanatzidis, A. Yartsev, *Nat. Commun.* **2017**, *8*, 14398.
[24] H. Muta, K. Kurosaki, S. Yamanaka, *J. Alloys Compd.* **2005**, *392*, 306.
[25] H. Muta, K. Kurosaki, S. Yamanaka, *J. Alloys Compd.* **2003**, *350*, 292.
[26] D. Srivastava, C. Norman, F. Azough, M. C. Schafer, E. Guilmeau, D. Kepaptsoglou, Q. M. Ramasse, G. Nicotra, R. Freer, *Phys. Chem. Chem. Phys.* **2016**, *18*, 26475.
[27] Y. Lin, C. Norman, D. Srivastava, F. Azough, L. Wang, M. Robbins, K. Simpson, R. Freer, I. A. Kinloch, *ACS Appl. Mater. Interfaces* **2015**, *7*, 15898.
[28] O. Okhay, S. Zlotnik, W. J. Xie, K. Orlinski, M. J. H. Gallo, G. Otero-Irurueta, A. J. S. Fernandes, D. A. Pawlak, A. Weidenkaff, A. Tkach, *Carbon* **2019**, *143*, 215.
[29] X. P. Feng, Y. C. Fan, N. Nomura, K. Kikuchi, L. J. Wang, W. Jiang, A. Kawasaki, *Carbon* **2017**, *112*, 169.
[30] W. H. Nam, B. B. Kim, S. G. Seo, Y. S. Lim, J. Y. Kim, W. S. Seo, W. K. Choi, H. H. Park, J. Y. Lee, *Nano Lett.* **2014**, *14*, 5104.
[31] D. Marrocchelli, L. X. Sun, B. Yildiz, *J. Am. Chem. Soc.* **2015**, *137*, 4735.
[32] J. U. Rahman, N. V. Du, W. H. Nam, W. H. Shin, K. H. Lee, W. S. Seo, M. H. Kim, S. Lee, *Sci. Rep.* **2019**, *9*, 8624.
[33] P. A. Zong, R. Hanus, M. Dylla, Y. S. Tang, J. C. Liao, Q. H. Zhang, G. J. Snyder, L. D. Chen, *Energy Environ. Sci.* **2017**, *10*, 183.
[34] R. Nunna, P. F. Qiu, M. J. Yin, H. Y. Chen, R. Hanus, Q. F. Song, T. S. Zhang, M. Y. Chou, M. T. Agne, J. Q. He, G. J. Snyder, X. Shi, L. D. Chen, *Energy Environ. Sci.* **2017**, *10*, 1928.
[35] a) G. J. Snyder, M. Christensen, E. Nishibori, T. Caillat, B. B. Iversen, *Nat. Mater.* **2004**, *3*, 458; b) G. S. Nolas, D. T. Morelli, T. M. Tritt, *Annu. Rev. Mater. Sci.* **1999**, *29*, 89.
[36] Y. Lin, J. Jin, O. Kusmartsevab, M. Song, *J. Phys. Chem. C* **2013**, *117*, 17237.
[37] K. A. Borup, E. S. Toberer, L. D. Zoltan, G. Nakatsukasa, M. Errico, J. P. Fleurial, B. B. Iversen, G. J. Snyder, *Rev. Sci. Instrum.* **2012**, *83*, 123902.